

# Efficient method for calculation of low-temperature phase boundaries

Lucas Svensson,<sup>1,2</sup> Babak Sadigh,<sup>3, a)</sup> Christine Wu,<sup>3</sup> and Paul Erhart<sup>1,2, b)</sup>

<sup>1)</sup>*Department of Physics and Astronomy, Chalmers University of Technology, SE 412 96 Gothenburg, Sweden*

<sup>2)</sup>*Wallenberg Initiative Materials Science for Sustainability, Chalmers University of Technology, 41926 Gothenburg, Sweden*

<sup>3)</sup>*Lawrence Livermore National Laboratory, 7000 East Avenue, Livermore, 94550, CA, USA*

(Dated: 7 May 2026)

Understanding phase stability and phase transformations is central to predicting material behavior under varying thermodynamic conditions. One of the earliest and most influential applications of density functional theory in materials science has been the prediction of pressure-induced phase transitions at 0 K. Extending these calculations to finite temperatures, however, requires accounting for thermal, quantum, and anharmonic contributions to the free energy, often at significant computational cost. In this work, we present a general and efficient framework for calculating low-temperature phase boundaries by combining the Clausius-Clapeyron equation with the quasi-harmonic approximation. This methodology requires a minimal number of calculations, while naturally incorporating internal degrees of freedom as well as quantum and low-order anharmonic effects. We illustrate the accuracy and efficiency of the approach by constructing the phase diagram of silica in the pressure range from  $-2$  GPa to 12 GPa and temperatures up to 1750 K. To this end, we employ a machine-learned interatomic potential trained on density functional theory reference data, enabling well-converged free energy estimates via efficient thermodynamic sampling and a rigorous comparison between the proposed framework and free energy integration.

## I. INTRODUCTION

Accurate phase diagrams are essential for understanding the behavior of materials under varying thermodynamic conditions. Predicting phase stability and phase transformations is consequently a cornerstone of materials science, with implications ranging from geology and planetary science to microelectronics and energy storage<sup>1–5</sup>. However, constructing phase diagrams from first principles is often a numerically intensive task, in particular when internal degrees of freedoms (DOFs), such as lattice distortions or sublattice relaxations, play a significant role in determining phase stability<sup>6,7</sup>.

Electronic structure methods such as density-functional theory (DFT) have proven powerful for predicting pressure-induced phase transitions at 0 K by comparing enthalpies across structures<sup>8</sup>. However, at finite temperatures, comparing Gibbs free energies across structures over wide ranges of temperatures and pressures can be challenging, as vibrational contributions to both enthalpy and entropy, including zero-point quantum contributions, need to be accounted for. These contributions are typically evaluated using methods such as the quasi-harmonic approximation (QHA)<sup>9</sup> or thermodynamic integration based on molecular dynamics (MD) simulations<sup>10,11</sup>. Approaches that provide effective harmonic models capturing anharmonic contributions at finite temperatures, such as temperature-dependent effective potential (TDEP)<sup>12</sup> or self-consistent phonon (SCPH) methods<sup>13,14</sup>, can extend the range of validity

of phonon-based free energy calculations to higher temperatures, but at considerably higher computational cost.

Moreover, the presence of soft modes or structural complexity can make phonon calculations particularly delicate, further increasing the computational burden. These challenges are especially pronounced in materials with complex bonding environments or multiple competing polymorphs. Silica ( $\text{SiO}_2$ ), for example, exhibits a rich array of pressure- and temperature-dependent phases, including tridymite, quartz, coesite, and stishovite, each with distinct structural motifs and vibrational properties<sup>15</sup>. Capturing the correct stability fields of such phases requires careful treatment of the vibrational entropy in addition to static lattice energetics.

In this work, we present a general and efficient framework for calculating low-temperature phase boundaries by combining a higher-order expansion of the Clausius-Clapeyron (CC) equation with a small number of QHA calculations. Quantum corrections (QC) are included via a perturbative treatment the terms of which are evaluated using harmonic phonon frequencies within the QHA. This accounts for zero-point energy and its effect on the critical pressure at low temperatures, but does not capture anharmonic quantum effects beyond those already implicit in the volume dependence of the QHA phonon frequencies. This framework significantly reduces the number of required calculations while naturally incorporating quantum effects and low-order anharmonicity for selected internal DOFs.

Due to its complex polymorphic landscape and well-studied pressure-temperature behavior, silica serves as an ideal test case for demonstrating our method, which we apply to construct its phase diagram from  $-2$  GPa to 12 GPa and up to 1750 K. To this end, we train a machine-learned interatomic potential (MLIP) of the neuroevolution potential (NEP) form<sup>16,17</sup> on first-

---

<sup>a)</sup>Electronic mail: sadigh1@llnl.gov

<sup>b)</sup>Electronic mail: erhart@chalmers.se

principles DFT data, and utilize it to perform both the phonon calculations required for our CC-QHA+QC framework and free energy integration, which serves as a reference when analyzing the CC-QHA+QC results. This approach enables efficient sampling of the thermodynamic space while retaining ab initio-level accuracy through the underlying training data.

Our results demonstrate the practical advantages of the CC-QHA+QC framework for efficiently predicting phase boundaries in materials with complex internal DOFs, including quantum effects. Crucially in the present work, the MLIP serves as a reference method that is sufficiently computationally efficient to enable a one-to-one comparison of the CC-QHA+QC approach with free energy integration. In practice, the CC-QHA+QC approach is computationally much less demanding than free energy integration, and naturally accommodates quantum corrections. Its computational efficiency makes it directly applicable in conjunction with DFT calculations.

## II. THEORY

The phase boundary  $P^*(T)$  between two phases denoted in the following by superscripts (1) and (2) is determined by the condition that their Gibbs free energies are equal:

$$G^{(2)}(P^*(T), T) = G^{(1)}(P^*(T), T).$$

The Gibbs free energy can be written as

$$\begin{aligned} G(P, T) &= F(V(P, T), T) + PV(P, T) \\ &= E(V, T) - TS(V, T) + PV(P, T), \end{aligned}$$

where  $V(P, T)$  denotes the dependence of the specific volume of a phase on pressure and temperature,  $F(V, T)$  is its Helmholtz free energy,  $E(V, T)$  its internal energy, and  $S(V, T)$  its entropy. For brevity in the following, we usually omit the explicit dependence of the specific volume  $V$  on pressure and temperature although it is always implied. The internal energy can be further decomposed into two contributions

$$E(V, T) = U_{\text{int}}(V) + E_{\text{vib}}(V, T), \quad (1)$$

where the first term on the right-hand side is the potential energy of the perfect lattice and the second term is the vibrational energy.

In the following, we first derive the temperature dependence of the transition pressure  $P^*(T)$  within classical statistical mechanics. Classical phase boundaries have finite derivatives  $dT/dP^*$  at 0 K and are therefore well described by a low-order Taylor expansion near 0 K. This is not true for the quantum mechanical phase boundaries, which are vertical in the  $T$ - $P$  plane at 0 K (i.e.,  $dT/dP^* \rightarrow \infty$ ). In Sect. IIB, we will show how we can derive the quantum phase boundary from the classical one.

### A. Classical statistics

In a classical system, at 0 K, the vibrational energy vanishes and the transition pressure  $P^*(0)$  satisfies the following equation

$$\begin{aligned} U_{\text{int}}^{(1)}(V^{(1)}(P^*)) + P^* V^{(1)}(P^*) &= \\ U_{\text{int}}^{(2)}(V^{(2)}(P^*)) + P^* V^{(2)}(P^*) & \end{aligned}$$

To determine the temperature-dependence of the transition pressure,  $P^*(T)$ , we carry out a second-order Taylor expansion in temperature,

$$P^*(T) = P^*(0) + \left. \frac{dP^*}{dT} \right|_{T=0} T + \frac{1}{2} \left. \frac{d^2 P^*}{dT^2} \right|_{T=0} T^2 + \mathcal{O}(T^3). \quad (2)$$

The first-order derivative can be obtained via the CC equation,

$$\frac{dP^*}{dT} = \frac{\Delta S_{\text{cl}}}{\Delta V}, \quad (3)$$

where  $\Delta S_{\text{cl}} = S_{\text{cl}}^{(2)} - S_{\text{cl}}^{(1)}$  and  $\Delta V = V^{(2)} - V^{(1)}$  are the differences in entropy and specific volume between the two considered phases, respectively.

In the classical 0 K limit, vibrations can be considered harmonic, and the classical vibrational entropy can be written as

$$S_{\text{cl}}(V) = -k_B \sum_{i=1}^{3N} \ln \omega_i(V), \quad (4)$$

where  $N$  is the number of atoms,  $\omega_i(V)$  is the volume-dependent angular frequency of the  $i$ -th phonon mode, and for brevity, we have omitted a benign temperature-dependent term  $3Nk_B [1 + \ln(2\pi k_B T/\hbar)]$ .

To evaluate the slope of the classical phase boundary  $dP^*/dT$  at 0 K,  $S_{\text{cl}}$  must be calculated for the two phases using Eq. (4) and substituted into Eq. (3).

It is possible to obtain higher-order derivatives of the phase boundary at 0 K. To this end, we differentiate Eq. (3) with respect to temperature, and for simplicity neglect the explicit temperature dependence of the entropy:

$$\begin{aligned} \frac{d^2 P^*}{dT^2} &= \frac{d}{dT} \left( \frac{\Delta S_{\text{cl}}}{\Delta V} \right) \\ &= \frac{1}{\Delta V} \left[ \frac{\partial V^{(2)}}{\partial T} \left( \frac{\partial S_{\text{cl}}^{(2)}}{\partial V} - \frac{dP^*}{dT} \right) \right. \\ &\quad \left. - \frac{\partial V^{(1)}}{\partial T} \left( \frac{\partial S_{\text{cl}}^{(1)}}{\partial V} - \frac{dP^*}{dT} \right) \right]. \end{aligned} \quad (5)$$

Note that in Eq. (5)  $S_{\text{cl}}^{(1)}(V^{(1)})$ ,  $S_{\text{cl}}^{(2)}(V^{(2)})$ , and their derivatives are calculated using Eq. (4), which amounts to the classical QHA. Within this approximation, the

thermal change of volume can be shown (see Appendix) to be

$$\left. \frac{\partial V}{\partial T} \right|_{T=0} = \frac{V}{B} \frac{\partial S_{\text{cl}}}{\partial V}, \quad (6)$$

where  $B$  is the bulk modulus at 0 K. Inserting this relation in Eq. (5), the second derivative of the phase boundary at 0 K can be written as

$$\frac{d^2 P^*}{dT^2} = \frac{1}{\Delta V} \left[ \frac{V^{(2)}}{B^{(2)}} \frac{\partial S_{\text{cl}}^{(2)}}{\partial V} \left( \frac{\partial S_{\text{cl}}^{(2)}}{\partial V} - \frac{dP^*}{dT} \right) - \frac{V^{(1)}}{B^{(1)}} \frac{\partial S_{\text{cl}}^{(1)}}{\partial V} \left( \frac{\partial S_{\text{cl}}^{(1)}}{\partial V} - \frac{dP^*}{dT} \right) \right]. \quad (7)$$

We now have all the ingredients for calculating the temperature dependence of a phase boundary to second order in the Taylor expansion Eq. (2), with all terms available via zero-temperature phonon calculations.

## B. Quantum statistics

At low temperatures, within the QHA, the quantum-corrected Helmholtz free energy can be written as

$$F_{\text{qm}}(V, T) = U_{\text{int}}(V) + \sum_{i=1}^{3N} \frac{1}{2} \hbar \omega_i(V) + \sum_{i=1}^{3N} k_B T \ln \left( 1 - e^{-\hbar \omega_i(V)/k_B T} \right), \quad (8)$$

where  $N$  is the number of atoms and  $\omega_i(V)$  is the angular frequency of the  $i$ -th phonon mode, which is allowed to be volume-dependent. The quantum vibrational entropy can be calculated via the relation

$$S_{\text{qm}} = - \frac{\partial F_{\text{qm}}}{\partial T}.$$

However, the strongly non-linear temperature-dependence of  $S_{\text{qm}}$  makes a low-order Taylor expansion as in Eq. (2) ineffective. A more appropriate perturbative expansion is in  $\delta P(T)$  defined as

$$\delta P(T) = P_{\text{qm}}^*(T) - P_{\text{cl}}^*(T), \quad (9)$$

assuming the magnitude of the quantum corrections to the phase boundary is small, which is a reasonable assumption in the majority of cases.

For brevity and without loss of generality, we omit the explicit temperature dependence of  $\delta P$  and the free energies in the following. We thus write the condition for two-phase coexistence as

$$G_{\text{qm}}^{(1)}(P_{\text{cl}}^* + \delta P) = G_{\text{qm}}^{(2)}(P_{\text{cl}}^* + \delta P). \quad (10)$$

A first-order expansion in  $\delta P$  yields

$$G_{\text{qm}}^{(1)}(P_{\text{cl}}^*) + V_{\text{qm}}^{(1)}(P_{\text{cl}}^*) \delta P = G_{\text{qm}}^{(2)}(P_{\text{cl}}^*) + V_{\text{qm}}^{(2)}(P_{\text{cl}}^*) \delta P, \quad (11)$$

where we have used the thermodynamic relation

$$\left. \frac{\partial G}{\partial P} \right|_{P^*} = V(P^*). \quad (12)$$

Equation (11) can now be solved to obtain a closed expression for  $\delta P$

$$P_{\text{qm}}^* = \frac{F_{\text{qm}}^{(2)}(V_{\text{qm}}^{(2)}(P_{\text{cl}}^*)) - F_{\text{qm}}^{(1)}(V_{\text{qm}}^{(1)}(P_{\text{cl}}^*))}{V_{\text{qm}}^{(1)}(P_{\text{cl}}^*) - V_{\text{qm}}^{(2)}(P_{\text{cl}}^*)} \quad (13)$$

The above equation is straightforward to evaluate once the quantum-corrected specific volumes  $V_{\text{qm}}(P_{\text{cl}}^*)$  have been calculated. They are solutions to the equation

$$P_{\text{cl}}^* = - \left. \frac{\partial F_{\text{qm}}}{\partial V} \right|_{V_{\text{qm}}} = - \dot{F}_{\text{qm}}(V_{\text{qm}}). \quad (14)$$

The above equation can be solved numerically by a simple root finding algorithm. However, it can also be solved by perturbation theory in orders of  $\delta V$  defined as

$$\delta V = V_{\text{qm}} - V_{\text{cl}}. \quad (15)$$

To zeroth order in  $\delta V$ , Eq. (13) becomes

$$P_{\text{qm}}^* = \frac{F_{\text{qm}}^{(2)}(V_{\text{cl}}^{(2)}) - F_{\text{qm}}^{(1)}(V_{\text{cl}}^{(1)})}{V_{\text{cl}}^{(1)} - V_{\text{cl}}^{(2)}}. \quad (16)$$

This level of approximation often suffices for description of the small quantum corrections that are found in common materials. However, for completeness, we conclude by showing how to derive higher-order terms in perturbation theory. We therefore rewrite Eq. (14)

$$P_{\text{cl}}^* = - \dot{F}_{\text{qm}}(V_{\text{cl}} + \delta V). \quad (17)$$

To first order in  $\delta V$ , the above equation can be solved to yield

$$\delta V = - \frac{P_{\text{cl}}^* + \dot{F}_{\text{qm}}(V_{\text{cl}})}{\ddot{F}_{\text{qm}}(V_{\text{cl}})}, \quad (18)$$

where  $\ddot{F}_{\text{qm}}$  is the second derivative of the Helmholtz free energy Eq. (8) with respect to volume. Note that the evaluation of  $\ddot{F}_{\text{qm}}$  requires calculation of the second derivatives of the phonon frequencies with respect to volume. Inserting now  $V_{\text{qm}} = V_{\text{cl}} + \delta V$  in Eq. (13), we can obtain  $P_{\text{qm}}^*$  to a higher order approximation.

To apply the CC-QHA+QC framework, i.e., to evaluate Eq. (2) with additional quantum corrections from Eq. (16), we require the following quantities:

- I. the transition pressure at zero temperature,  $P_{\text{cl}}^*(0)$
- II. the entropy and volume differences between the two phases to evaluate Eq. (3)
- III. the derivative of the entropy with respect to volume and the bulk modulus at the transition pressure to calculate Eq. (7)

IV. the quantum mechanical free energy difference as a function of classical volume, to account for quantum effects using Eq. (16).

While we use volume as the varying QHA-DOF in this work, the CC-QHA+QC framework is general and may be extended to any internal DOFs. This includes, for example, symmetry-preserving lattice distortions or sublattice relaxations where the free-energy landscape can be parameterized as a function of such coordinates.

In summary, the CC-QHA+QC framework rests on three approximations. First, the temperature dependence of the transition pressure is captured by a second-order Taylor expansion, which is justified at low temperatures where higher-order anharmonic contributions are small. Second, thermal expansion and entropy are evaluated within the QHA, in which phonon frequencies depend on volume but not explicitly on temperature. Third, quantum corrections to the transition pressure are included perturbatively to first order in  $\hbar$ , which is accurate when quantum corrections to the equilibrium volume are small. Together, these approximations enable the phase boundary to be reconstructed from a small number of phonon calculations at 0 K, without recourse to MD simulations or full free energy surfaces.

### III. METHODS

#### Interatomic potential and DFT calculations

To demonstrate the CC-QHA+QC framework and to provide a reference via free energy integration, we constructed a MLIP of the NEP form<sup>16–19</sup> using an active learning strategy<sup>20</sup> based on DFT calculations with the r2SCAN exchange-correlation functional<sup>21</sup> (see Supplementary Note S1 and Supplementary Note S2 for full details of the model construction<sup>22,23</sup> and DFT settings<sup>24–28</sup>). The training set consisted of 1218 structures covering crystalline and amorphous configurations of SiO<sub>2</sub> and Si across a range of pressures and temperatures. The final model achieves root mean square errors (RMSEs) of 20 meV/atom for energies and 273 meV/Å for forces, with coefficients of determination  $R^2 > 0.99$  in both cases (Fig. 1 and Supplementary Note S1). The energy–volume curves and enthalpy differences predicted by the NEP model are in very good agreement with the underlying DFT reference data (see Fig. S4 and Fig. S5), confirming that the model faithfully reproduces the energy landscape relevant for the phase boundaries studied here. We note that the level of agreement with experiment<sup>29</sup> observed below should be attributed primarily to the r2SCAN functional used in the training data. The MLIP models and DFT reference data are available on Zenodo at <https://doi.org/10.5281/zenodo.14925353>.

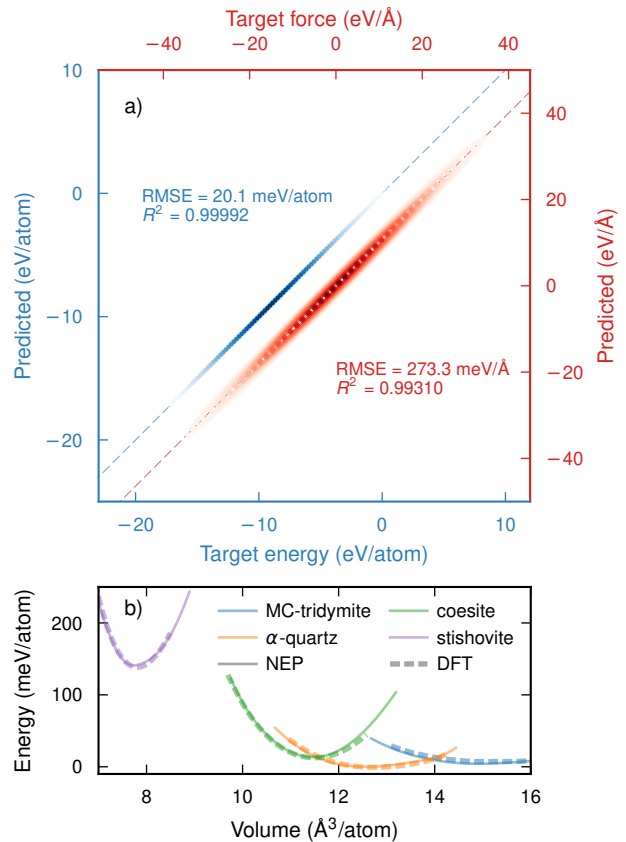


FIG. 1. (a) Parity plots comparing energies and forces predicted by the MLIP model constructed in this work against DFT reference data. (b) Energy–volume curves computed using the MLIP model, shown alongside corresponding results from DFT calculations for validation.

#### Clausius-Clapeyron relation and quasi-harmonic approximation

To efficiently compute phase boundaries at low temperatures, we combine the CC equation (3) with QHA phonon calculations. This approach captures quantum effects and anharmonic corrections while requiring only a limited set of force calculations (Sect. II). In contrast to conventional QHA-based phase diagram construction, which requires full free energy surfaces, the CC-QHA+QC approach reconstructs phase boundaries from local thermodynamic derivatives, significantly reducing computational cost.

The transition pressure at zero temperature,  $P^*(0)$ , (see step I in workflow in Eq. IIB) was determined by computing the enthalpy as a function of pressure for each phase and identifying the transition pressure at which their enthalpy curves intersect (see Fig. S4 of the Supplementary Material).

To compute the volume and entropy differences (step II), structures of each phase relaxed at  $P^*(0)$  were used. The force constants were determined using

the HIPHIVE package<sup>23</sup> and subsequently passed to the PHONOPY package<sup>30,31</sup> to compute the classical entropy of each phase.

The entropy derivative and bulk modulus (step III) were evaluated using structures with volumes 0.2% above and below that of the structures relaxed at  $P^*(0)$ . The entropy derivative was obtained through numerical differentiation as

$$\left. \frac{\partial S}{\partial V} \right|_{V_0} = \frac{S(V_0 + \delta V) - S(V_0 - \delta V)}{2\delta V}$$

and the bulk modulus as

$$B = -V_0 \left. \frac{dP}{dV} \right|_{V_0} = -V_0 \frac{P(V_0 + \delta V) - P(V_0 - \delta V)}{2\delta V}.$$

The classical and quantum mechanical free energy differences between the phases (step IV) were then calculated using the same set of force constants in combination with PHONOPY.

#### Free energy integration and molecular dynamics

To validate the CC-QHA+QC framework, the phase diagram was additionally constructed via free energy integration using MD simulations. To this end, we performed thermodynamic integration using both adiabatic switching<sup>32</sup> and reversible scaling<sup>11,33</sup> as implemented in GPUMD<sup>17,18</sup>. To obtain the second-order transition boundary between  $\alpha$ -quartz and  $\beta$ -quartz, standard MD simulations were conducted at various pressures (Fig. S1 and Fig. S6 in the Supplementary Material). The heat capacities exhibit a pronounced peak at the  $\alpha$ - $\beta$ -quartz transition temperature (Fig. S1b), which yields the phase boundary as a function of pressure.

## IV. RESULTS

Figure 2 compares phase diagrams for SiO<sub>2</sub> obtained using the CALPHAD approach based on experimental data<sup>15</sup> as well as using the NEP model via free energy integration and the CC-QHA+QC framework introduced here, respectively. We first observe that the NEP model predicts a phase diagram in good agreement with experiment (Fig. 2a). The low-pressure transition between tridymite and  $\alpha$ -quartz, as well as the high-pressure transition between coesite and stishovite, are found to be in near-quantitative agreement. However, slight deviations are observed for the transition between  $\alpha$ -quartz and coesite, resulting in a modest overstabilization of the  $\alpha$ -quartz and  $\beta$ -quartz phases. Both the agreement and the remaining deviations should be attributed to the underlying exchange-correlation functional. This assessment is supported by the observation that the MLIP constructed in Ref. 34 using a different MLIP format and training set,

albeit using a closely related exchange-correlation functional, predicts a phase diagram that resembles the one obtained via the NEP model here.

Since the phonon calculations used to predict the phase diagram within our CC-QHA+QC framework (Fig. 2b) are based on the NEP model, the phase diagram obtained via free energy integration serves as a natural reference for assessing the accuracy of our approach. This comparison shows that the CC-QHA+QC framework predicts the phase boundaries between tridymite and  $\alpha$ -quartz as well as between  $\alpha$ -quartz and coesite in excellent agreement with the reference phase diagram. With respect to the stishovite-coesite transition, the CC-QHA+QC approach, however, yields a boundary with a somewhat flatter slope. It should be noted that the boundary between  $\alpha$ - and  $\beta$ -quartz marks a continuous transition that is not numerically accessible from free energies, and therefore cannot be captured by the CC-QHA+QC approach.

The accuracy of the CC-QHA+QC framework is bounded by the applicability of the QHA and the low-temperature Taylor expansion; the method is not expected to remain accurate when anharmonic contributions become significant. For the tridymite-quartz and quartz-coesite boundaries, the framework remains in excellent agreement with the free energy integration reference up to the highest temperatures considered here ( $\sim 1500$  K). In the case of the coesite-stishovite boundary, deviations become noticeable already around 600 K, which we attribute to the unusually large contrast in vibrational stiffness between the two phases, evident from both the phonon dispersions (Fig. 3) and the elastic constants (Table S5), that amplifies anharmonic contributions. Methods that provide effective harmonic models at finite temperatures, such as TDEP<sup>12</sup> or SCPH approaches<sup>13,14</sup>, could in principle supply improved force constants as input to the present framework, potentially extending its range of applicability to higher temperatures.

It is also apparent that the CC-QHA+QC approach yields a noticeable and consistent improvement compared to the classical CC relation (red lines in Fig. 2b). This effect is most evident for the  $\alpha$ -quartz-coesite and tridymite- $\alpha$ -quartz boundaries, for the latter of which the CC relation even yields the wrong slope.

Examining the low-temperature region of the coesite-stishovite boundary (Fig. 2b) highlights the importance of incorporating quantum effects within the CC-QHA+QC framework. When quantum effects are neglected, the boundary exhibits a finite slope  $dT/dP^*$  at 0 K, whereas the inclusion of quantum effects correctly, and as expected from thermodynamic principles, drives this slope to infinity (i.e., the boundary becomes vertical in the  $T$ - $P$  plane), consistent with the vanishing of the quantum mechanical entropies of both phases at 0 K as dictated by Eq. (3).

The phonon dispersions (Fig. 3) reveal that stishovite exhibits significantly fewer low-frequency phonon modes compared to coesite, indicating a higher vibrational stiff-

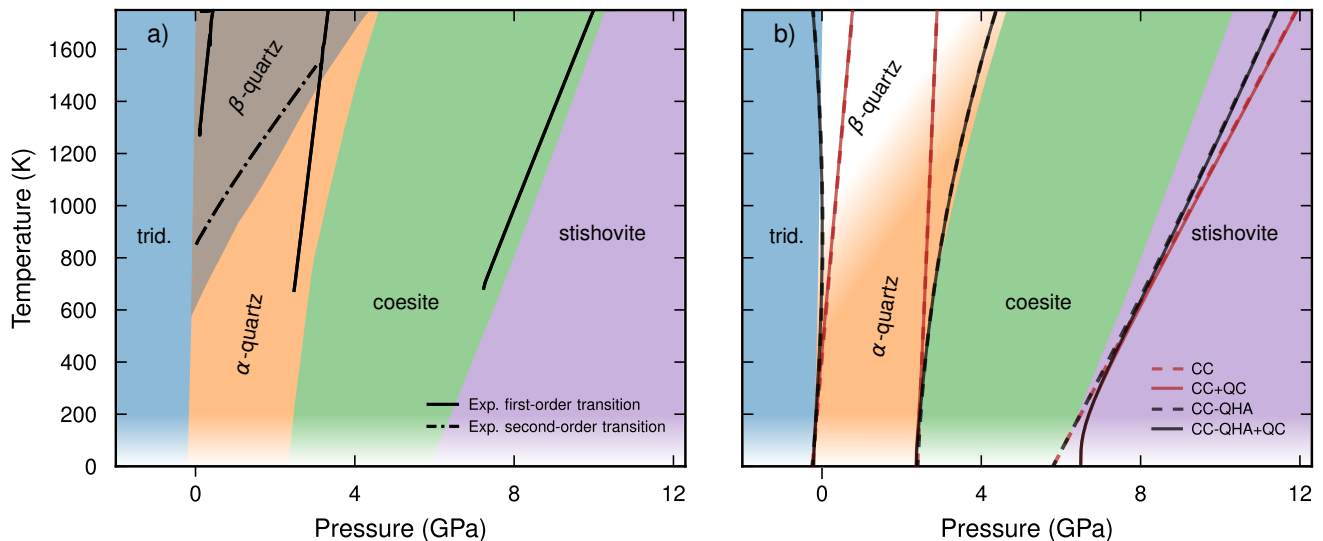


FIG. 2. Temperature–pressure phase diagram of  $\text{SiO}_2$ . Colored regions indicate the phase diagram predicted using free energy integration based on the NEP model. The faded low-temperature region marks the lowest temperature at which free energy integration remains accurate. (a) Phase boundaries adapted from experimental data reported in Ref. 15. (b) Phase boundaries obtained using first-order expansion without QC (CC), first-order expansion with QC (CC+QC), second-order expansion without QC (CC-QHA), and second-order expansion with QC (CC-QHA+QC).

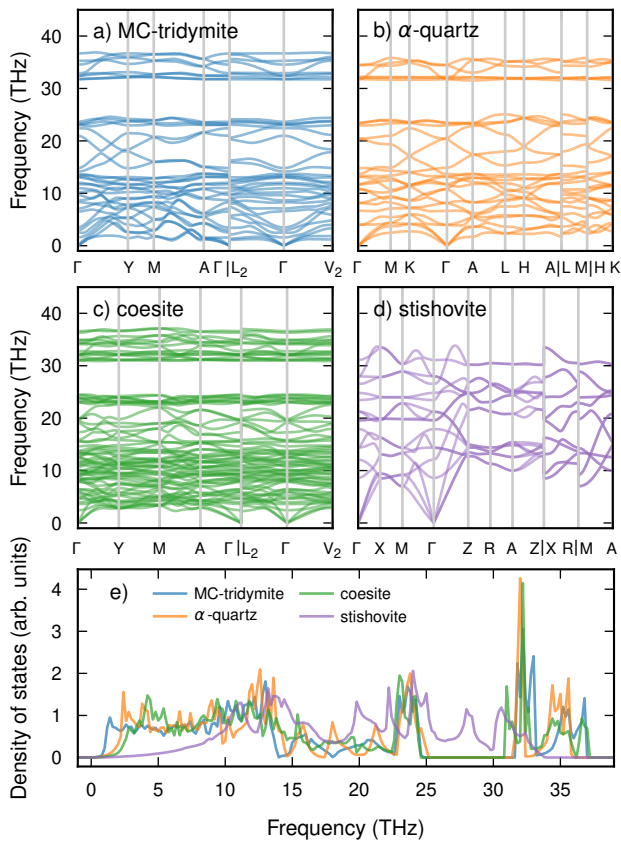


FIG. 3. Phonon dispersion relations of (a) tridymite, (b)  $\alpha$ -quartz, (c) coesite, and (d) stishovite, along with (e) the corresponding phonon densities of states for all four structures.

ness, which is also visible in the elastic constants (Table S5). This stiffer character leads to a smaller vibrational entropy at low temperatures. Consequently, the larger entropy difference between the two phases leads to a stronger temperature dependence of the transition pressure, further highlighting the relevance of quantum effects in accurately describing this phase boundary.

## V. CONCLUSIONS

We have introduced a framework that combines the Clausius-Clapeyron equation with the quasi-harmonic approximation and quantum corrections (CC-QHA+QC) and demonstrated that it provides an efficient and accurate method for determining phase boundaries in solid-phase systems. In particular, we have shown that this approach captures the thermodynamic behavior of  $\text{SiO}_2$  polymorphs across a wide range of pressures and temperatures.

Compared to free energy integration methods based on MD, the CC-QHA+QC framework reduces the computational cost substantially while yielding comparable accuracy. In principle, only six phonon calculations, three per phase, are required to map out a two-phase boundary, making the method directly applicable with DFT calculations. Free energy integration, by contrast, requires extensive MD sampling at each state point, making it impractical to perform directly with DFT; the use of MLIPs makes this task more tractable but requires prior model construction. Moreover, incorporating quantum nuclear effects in free energy integration requires path-integral MD simulations, increasing the computational effort by

roughly an order of magnitude. The CC-QHA+QC approach therefore strikes a balance between efficiency, accuracy, and natural incorporation of quantum effects, making it well suited for applications that require DFT-level accuracy or high-throughput phase boundary calculations.

Importantly, and as expected from thermodynamic principles, the inclusion of quantum vibrational effects within the CC-QHA+QC framework correctly reproduces the infinite slope of phase boundaries at zero temperature. This is especially relevant for systems where the vibrational entropy differs strongly between neighboring phases (exemplified by the coesite–stishovite boundary), influencing the shape and location of the phase boundaries. Crucially, this is achieved without recourse to path-integral MD simulations, by incorporating the quantum correction via the zero-point free energy difference at the QHA level.

The accuracy of the framework is bounded by the validity of the QHA and the low-temperature Taylor expansion. In the present application to silica, excellent agreement with the free energy integration reference is obtained up to  $\sim 1500$  K for the tridymite– $\alpha$ -quartz and  $\alpha$ -quartz–coesite boundaries. For the coesite–stishovite boundary, deviations become apparent around 600 K, likely due to the large stiffness contrast between those phases. Replacing the QHA force constants with temperature-dependent ones from TDEP<sup>12</sup> or SCPH<sup>13,14</sup> could extend the approach to more strongly anharmonic systems or higher temperatures.

Although volume is the only quasi-harmonic DOF considered in this work, the CC-QHA+QC framework is generalizable to any number of internal coordinates that can be treated within the QHA.

## Appendix A: Relationship for thermal expansion coefficient

In this section, we show that within the QHA approximation, Eq. (6) is satisfied. We start with the expression for the pressure within QHA

$$P(T) = -\frac{\partial U_{\text{int}}}{\partial V} + T \frac{\partial S_{\text{cl}}}{\partial V}, \quad (\text{A1})$$

where  $U_{\text{int}}$  and  $S_{\text{cl}}$  are defined in Sect. II A. Now, under isobaric conditions, the temperature dependence of the specific volume follows from the constant-pressure condition. At 0 K, we thus have

$$0 = \left. \frac{dP}{dT} \right|_{T=0} = -\frac{\partial^2 U_{\text{int}}}{\partial V^2} \frac{\partial V}{\partial T} \Big|_{T=0} + \frac{\partial S_{\text{cl}}}{\partial V}. \quad (\text{A2})$$

Solving the above equation, using the relation

$$\frac{B}{V} = \frac{\partial^2 U_{\text{int}}}{\partial V^2}, \quad (\text{A3})$$

we obtain Eq. (6).

## SUPPLEMENTARY MATERIAL

The supplementary material provides further details on the training of the NEP model and the DFT calculations used to generate the training data, as well as benchmark results, including parity plots, energy-volume curves, thermal expansion, and phonon dispersions.

## ACKNOWLEDGMENTS

This work was supported by the Swedish Research Council (Nos. 2020-04935, 2021-05072, and 2025-03999) and the Wallenberg Initiative Materials Science for Sustainability. Part of this work was performed under the auspices of the US Department of Energy by Lawrence Livermore National Laboratory under Contract DE-AC52-07NA27344. Some of the computations were enabled by resources provided by the National Academic Infrastructure for Supercomputing in Sweden (NAISS) at PDC, C3SE, and NSC, partially funded by the Swedish Research Council through grant agreement no. 2022-06725 as well as the Berzelius resource provided by the Knut and Alice Wallenberg Foundation at NSC.

## CONFLICT OF INTEREST

The authors have no conflicts to disclose.

## DATA AVAILABILITY

The MLIP model, including the model ensemble constructed in this work as well as the DFT reference data used for its construction, are available on Zenodo at <https://doi.org/10.5281/zenodo.14925353>.

- <sup>1</sup>R. Jeanloz and A. B. Thompson, “Phase transitions and mantle discontinuities,” *Reviews of Geophysics* **21**, 51–74 (1983).
- <sup>2</sup>F. Coppari, R. F. Smith, J. H. Eggert, J. Wang, J. R. Rygg, A. Lazicki, J. A. Hawreliak, G. W. Collins, and T. S. Duffy, “Experimental evidence for a phase transition in magnesium oxide at exoplanet pressures,” *Nature Geoscience* **6**, 926–929 (2013).
- <sup>3</sup>C. Zheng, R. E. Simpson, K. Tang, Y. Ke, A. Nemati, Q. Zhang, G. Hu, C. Lee, J. Teng, J. K. Yang, J. Wu, and C.-W. Qiu, “Enabling Active Nanotechnologies by Phase Transition: From Electronics, Photonics to Thermotics,” *Chemical Reviews* **122**, 15450–15500 (2022).
- <sup>4</sup>Y. Tian, L. Jin, H. Zhang, Z. Xu, X. Wei, G. Viola, I. Abrahams, and H. Yan, “Phase transitions in bismuth-modified silver niobate ceramics for high power energy storage,” *Journal of Materials Chemistry A* **5**, 17525–17531 (2017).
- <sup>5</sup>T. Hainer, E. Fransson, S. Dutta, J. Wiktor, and P. Erhart, “A morphotropic phase boundary in  $\text{MA}_{1-x}\text{FA}_x\text{PbI}_3$ : Linking structure, dynamics, and electronic properties,” *Nature Communications* **16**, 8775 (2025).
- <sup>6</sup>T. Schwabe and S. Grimme, “Theoretical Thermodynamics for Large Molecules: Walking the Thin Line between Accuracy and Computational Cost,” *Accounts of Chemical Research* **41**, 569–579 (2008).

- <sup>7</sup>X.-G. Zhao, G. M. Dalpian, Z. Wang, and A. Zunger, “Polymorphous nature of cubic halide perovskites,” *Physical Review B* **101**, 155137 (2020).
- <sup>8</sup>L. Gracia, A. Beltrán, and J. Andrés, “Characterization of the High-Pressure Structures and Phase Transformations in SnO<sub>2</sub>. A Density Functional Theory Study,” *The Journal of Physical Chemistry B* **111**, 6479–6485 (2007).
- <sup>9</sup>J. D. Althoff, P. B. Allen, R. M. Wentzcovitch, and J. A. Moriarty, “Phase diagram and thermodynamic properties of solid magnesium in the quasiharmonic approximation,” *Physical Review B* **48**, 13253–13260 (1993).
- <sup>10</sup>T. P. Straatsma and H. J. C. Berendsen, “Free energy of ionic hydration: Analysis of a thermodynamic integration technique to evaluate free energy differences by molecular dynamics simulations,” *The Journal of Chemical Physics* **89**, 5876–5886 (1988).
- <sup>11</sup>R. Freitas, M. Asta, and M. de Koning, “Nonequilibrium free-energy calculation of solids using LAMMPS,” *Computational Materials Science* **112**, 333–341 (2016).
- <sup>12</sup>O. Hellman, I. A. Abrikosov, and S. I. Simak, “Lattice dynamics of anharmonic solids from first principles,” *Physical Review B* **84**, 180301 (2011).
- <sup>13</sup>T. Tadano and S. Tsuneyuki, “Self-consistent phonon calculations of lattice dynamical properties in cubic SrTiO<sub>3</sub> with first-principles anharmonic force constants,” *Physical Review B* **92**, 054301 (2015).
- <sup>14</sup>E. Fransson, P. Rosander, F. Eriksson, J. M. Rahm, T. Tadano, and P. Erhart, “Limits of the phonon quasi-particle picture at the cubic-to-tetragonal phase transition in halide perovskites,” *Communications Physics* **6**, 173 (2023).
- <sup>15</sup>V. Swamy, S. K. Saxena, B. Sundman, and J. Zhang, “A thermodynamic assessment of silica phase diagram,” *Journal of Geophysical Research: Solid Earth* **99**, 11787–11794 (1994).
- <sup>16</sup>Z. Fan, Z. Zeng, C. Zhang, Y. Wang, K. Song, H. Dong, Y. Chen, and T. Ala-Nissila, “Neuroevolution machine learning potentials: Combining high accuracy and low cost in atomistic simulations and application to heat transport,” *Physical Review B* **104**, 104309 (2021).
- <sup>17</sup>Z. Fan, Y. Wang, P. Ying, K. Song, J. Wang, Y. Wang, Z. Zeng, K. Xu, E. Lindgren, J. M. Rahm, A. J. Gabourie, J. Liu, H. Dong, J. Wu, Y. Chen, Z. Zhong, J. Sun, P. Erhart, Y. Su, and T. Ala-Nissila, “GPUMD: A package for constructing accurate machine-learned potentials and performing highly efficient atomistic simulations,” *The Journal of Chemical Physics* **157**, 114801 (2022).
- <sup>18</sup>K. Xu, H. Bu, S. Pan, E. Lindgren, Y. Wu, Y. Wang, J. Liu, K. Song, B. Xu, Y. Li, T. Hainer, L. Svensson, J. Wiktor, R. Zhao, H. Huang, C. Qian, S. Zhang, Z. Zeng, B. Zhang, B. Tang, Y. Xiao, Z. Yan, J. Shi, Z. Liang, J. Wang, T. Liang, S. Cao, Y. Wang, P. Ying, N. Xu, C. Chen, Y. Zhang, Z. Chen, X. Wu, W. Jiang, E. Berger, Y. Li, S. Chen, A. J. Gabourie, H. Dong, S. Xiong, N. Wei, Y. Chen, J. Xu, F. Ding, Z. Sun, T. Ala-Nissila, A. Harju, J. Zheng, P. Guan, P. Erhart, J. Sun, W. Ouyang, Y. Su, and Z. Fan, “Gpumd 4.0: A high-performance molecular dynamics package for versatile materials simulations with machine-learned potentials,” *Materials Genome Engineering Advances* **3**, e70028 (2025).
- <sup>19</sup>E. Lindgren, J. M. Rahm, E. Fransson, F. Eriksson, N. Österbacka, Z. Fan, and P. Erhart, “calorine: A python package for constructing and sampling neuroevolution potential models,” *Journal of Open Source Software* **9**, 6264 (2024).
- <sup>20</sup>E. Fransson, J. Wiktor, and P. Erhart, “Phase Transitions in Inorganic Halide Perovskites from Machine-Learned Potentials,” *The Journal of Physical Chemistry C* **127**, 13773–13781 (2023).
- <sup>21</sup>J. W. Furness, A. D. Kaplan, J. Ning, J. P. Perdew, and J. Sun, “Accurate and Numerically Efficient r2SCAN Meta-Generalized Gradient Approximation,” *The Journal of Physical Chemistry Letters* **11**, 8208–8215 (2020).
- <sup>22</sup>A. Larsen, J. Mortensen, J. Blomqvist, I. Castelli, R. Christensen, M. Dulak, J. Friis, M. Groves, B. Hammer, C. Hargus, E. Hermes, P. Jennings, P. Jensen, J. Kermode, J. Kitchin, E. Kolsbjerg, J. Kubal, K. Kaasbjerg, S. Lysgaard, J. Maronsson, T. Maxson, T. Olsen, L. Pastewka, A. Peterson, C. Rostgaard, J. Schiøtz, O. Schütt, M. Strange, K. Thygesen, T. Vegge, L. Vilhelmsen, M. Walter, Z. Zeng, and K. W. Jacobsen, “The Atomic Simulation Environment – A Python library for working with atoms,” *J. Phys. Condens. Matter* **29**, 273002 (2017).
- <sup>23</sup>F. Eriksson, E. Fransson, and P. Erhart, “The Hiphive Package for the Extraction of High-Order Force Constants by Machine Learning,” *Advanced Theory and Simulations* **2**, 1800184 (2019).
- <sup>24</sup>P. E. Blöchl, “Projector augmented-wave method,” *Physical Review B* **50**, 17953–17979 (1994).
- <sup>25</sup>G. Kresse and D. Joubert, “From ultrasoft pseudopotentials to the projector augmented-wave method,” *Physical Review B* **59**, 1758–1775 (1999).
- <sup>26</sup>G. Kresse and J. Hafner, “Ab initio molecular dynamics for liquid metals,” *Physical Review B* **47**, 558–561 (1993).
- <sup>27</sup>G. Kresse and J. Furthmüller, “Efficient iterative schemes for ab initio total-energy calculations using a plane-wave basis set,” *Physical Review B* **54**, 11169 (1996).
- <sup>28</sup>G. Kresse and J. Furthmüller, “Efficiency of ab-initio total energy calculations for metals and semiconductors using a plane-wave basis set,” *Computational Materials Science* **6**, 15 (1996).
- <sup>29</sup>I. G. Polyakova, “4. The Main Silica Phases and Some of Their Properties,” in *4. The Main Silica Phases and Some of Their Properties* (De Gruyter, 2014) pp. 197–268.
- <sup>30</sup>A. Togo, “First-principles Phonon Calculations with Phonopy and Phono3py,” *Journal of the Physical Society of Japan* **92**, 012001 (2023).
- <sup>31</sup>A. Togo, L. Chaput, T. Tadano, and I. Tanaka, “Implementation strategies in phonopy and phono3py,” *Journal of Physics: Condensed Matter* **35**, 353001 (2023), publisher: IOP Publishing.
- <sup>32</sup>D. Frenkel and A. J. C. Ladd, “New Monte-Carlo method to compute the free-energy of arbitrary solids - application to the fcc and hcp phases of hard-spheres,” *Journal of Chemical Physics* **81**, 3188–3193 (1984).
- <sup>33</sup>M. de Koning, A. Antonelli, and S. Yip, “Optimized free-energy evaluation using a single reversible-scaling simulation,” *Physical Review Letters* **83**, 3973 (1999).
- <sup>34</sup>L. C. Erhard, J. Rohrer, K. Albe, and V. L. Deringer, “Modelling atomic and nanoscale structure in the silicon–oxygen system through active machine learning,” *Nature Communications* **15**, 1927 (2024).

## Supplementary Material:

# Efficient method for calculation of low-temperature phase boundaries

Lucas Svensson<sup>1,2</sup>, Babak Sadigh<sup>3</sup>, Christine Wu<sup>3</sup>, and Paul Erhart<sup>1,2</sup>

<sup>1</sup>*Department of Physics and Astronomy, Chalmers University of Technology, 41926 Gothenburg, Sweden*

<sup>2</sup>*Wallenberg Initiative Materials Science for Sustainability, Chalmers University of Technology, 41926 Gothenburg, Sweden*

<sup>3</sup>*Lawrence Livermore National Laboratory, 7000 East Avenue, Livermore, 94550, CA, USA*

## Contents

<b>Supplementary Notes</b>	<b>1</b>
S1. Construction of the Machine-learned interatomic potential . . . . .	1
S2. Density functional theory calculations . . . . .	2
<b>Supplementary Tables</b>	<b>2</b>
S1. Parity statistics for NEP model for energies, forces, and virials . . . . .	2
S2. Energy differences for silicon structures from DFT and NEP model . . . . .	3
S3. Energy differences for silica structures from DFT and NEP model . . . . .	3
S4. Elastic stiffness tensors of silicon structures from NEP model . . . . .	3
S5. Elastic stiffness tensors of silica structures from NEP model . . . . .	4
<b>Supplementary Figures</b>	<b>5</b>
S1. Thermal expansion and heat capacity of quartz . . . . .	5
S2. Training of NEP model . . . . .	5
S3. Parity plots for NEP model . . . . .	6
S4. Enthalpy-pressure curves from DFT and NEP model . . . . .	6
S5. Energy-volume and pressure-volume curves from DFT and NEP model . . . . .	7
S6. Temperature-dependent properties from NEP-MD simulations . . . . .	7
S7. Phonon dispersions for silica structures from NEP model . . . . .	8
S8. Phonon dispersions for silicon structures from NEP model . . . . .	8

---

## Supplementary Notes

### Supplementary Note S1: Construction of the Machine-learned interatomic potential

The machine-learned interatomic potential (MLIP) model was constructed using the neuroevolution potential (NEP) framework [1–3] following the iterative active learning strategy described in Ref. 4, utilizing the GPUMD [2] and CALORINE [5] packages. Training structures included both crystalline and amorphous configurations of SiO<sub>2</sub> and Si (see Table S1 for a breakdown by structure type), representing a range of system sizes and supercell shapes. To this end, MLIP–molecular dynamics (MD) simulations were carried out between 300 and 3200 K and at pressures ranging from –1 to 20 GPa using the most recent generation of the NEP model at each iteration. Snapshots were randomly selected from these trajectories, for which reference energies, forces, and stresses were computed via density functional theory (DFT). These configurations were then included when training the next-generation NEP model. In total, the training set consisted of 1218 structures, and the final

model was obtained after 4 iterations. Structure generation and manipulation were carried out using the ASE [6] and HIPHIVE [7] packages.

The root mean square errors (RMSEs) for energies, forces, and stresses for the final model are  $20.1 \text{ meV atom}^{-1}$ ,  $273 \text{ meV \AA}^{-1}$ , and  $1.0 \text{ GPa}$ , respectively, with coefficients of determination of  $0.99992$ ,  $0.993$ , and  $0.990$ , respectively (see also Table S1 and Fig. S3). To estimate the model uncertainty, an ensemble model was trained using five folds each comprising a randomized selection of 90% of the available structures (bagging,  $k$ -fold cross-validation). The resulting RMSEs are  $43(13) \text{ meV atom}^{-1}$  for energies and  $319(64) \text{ meV \AA}^{-1}$  for forces, with average coefficients of determination of  $R^2 = 0.9995(4)$  and  $R^2 = 0.9896(48)$ , respectively. The MLIP models in a format suitable for the GPUMD package are available on Zenodo at <https://doi.org/10.5281/zenodo.14925353>; the record also includes the DFT reference data in the form of an ASE sqlite database.

## Supplementary Note S2: Density functional theory calculations

DFT calculations were performed using the projector augmented wave method [8, 9] as implemented in the Vienna ab-initio simulation package [10–12] with a plane wave energy cutoff of  $520 \text{ eV}$  and the rSCAN meta-generalized-gradient exchange-correlation functional [13]. The Brillouin zone was sampled with automatically generated  $\mathbf{k}$ -point grids with a maximum spacing of  $0.2 \text{ \AA}^{-1}$  and Gaussian smearing with a width of  $0.1 \text{ eV}$ . For the calculation of the forces, a finer support grid was employed to improve their numerical accuracy.

## Supplementary Tables

**Table S1: Parity statistics for NEP model for energies, forces, and virials.** Performance metrics including the coefficients of determination  $R^2$  and the RMSE for energies, forces, and virials for each structure type in the reference set obtained via the machine-learned interatomic potential of the NEP form compared to DFT calculations. Data shown are for the model trained against all available reference data.  $N$ : Number of data points.

	Energy ( $\text{meV atom}^{-1}$ )			Forces ( $\text{meV \AA}^{-1}$ )			Virial ( $\text{meV atom}^{-1}$ )		
	$R^2$	RMSE	$N$	$R^2$	RMSE	$N$	$R^2$	RMSE	$N$
all	0.99992	20.1	1218	0.9931	273.3	103638	0.9972	107.5	7308
rattled	0.99994	3.4	156	0.9991	153.4	28512	0.9995	32.1	936
dimer	0.99998	11.7	198	0.9982	220.2	5652	0.9996	99.3	1188
mp	0.99943	31.4	336	0.9138	222.9	36231	0.8607	147.1	2016
SiO <sub>2</sub>									
$\alpha$ -quartz-1	0.99896	13.2	51	0.9934	331.7	5913	0.9970	40.2	306
$\alpha$ -quartz-2	0.99938	11.2	48	0.9942	344.4	5265	0.9979	39.4	288
MC-tridymite	0.99974	23.4	49	0.9919	353.7	4140	0.9015	262.4	294
coesite	0.99944	10.1	49	0.9942	317.8	8280	0.9979	39.7	294
stishovite	0.99918	9.3	49	0.9907	332.7	3654	0.9960	70.5	294
$\alpha$ -cristobalite	0.99966	17.2	49	0.9934	357.2	7308	0.9949	58.9	294
$\alpha$ -tridymite	0.99890	12.4	47	0.9953	286.7	3852	0.9984	32.7	282
$\beta$ -quartz-1	0.99997	1.7	39	0.9993	129.8	3321	0.9994	24	234
$\beta$ -quartz-2	0.99996	2	39	0.9993	129.7	3321	0.9994	24.8	234
$\beta$ -cristobalite	0.99517	27.2	23	0.9923	404.8	1602	0.9897	123.7	138
$\beta$ -tridymite	0.99936	10.5	49	0.9938	323.4	4140	0.9979	50.2	294
keatite	0.98791	1.7	23	–	50.9	2484	0.9977	11.3	138
Si									
bc8	0.99755	15.3	36	0.9343	277.2	4104	0.9979	30.4	216
$\beta$ -tin	0.99732	12	34	0.9512	289.7	1878	0.9949	48.4	204
fcc	0.95923	22	48	0.9531	211.2	2097	0.9955	45.1	288
lonsdaleite	0.99847	2.3	27	–	95.0	324	0.9981	34	162
simple-hexagonal	0.99865	1.9	24	–	–	72	0.9986	26.2	144
diamond	0.99936	9.8	51	0.9812	231.0	4770	0.9961	52.8	306
Si <sub>2</sub>	0.99996	22	126	0.9876	312.6	15528	0.9993	117.2	756
O <sub>2</sub>	0.99995	15.1	620	0.9945	300.4	58431	0.9941	105.4	3720
SiO	0.99997	10.7	50	0.9996	253.6	303	0.9996	106.3	300

**Table S2: Energy differences for silicon structures from DFT and NEP model.** Energies from DFT and NEP calculations evaluated at the volume that minimizes the energy for each structure. Energies are reported relative to the lowest-energy structure. Data shown are for the model trained against all available reference data.

Structure (Si)	DFT (meV atom <sup>-1</sup> )	NEP (meV atom <sup>-1</sup> )
diamond	0.0	0.0
lonsdaleite	12.9	8.5
bc8	188.7	188.0
$\beta$ -tin	435.4	435.8
simple-hexagonal	449.7	447.3
fcc	748.0	746.5

**Table S3: Energy differences for silica structures from DFT and NEP model.** Energies from DFT and NEP calculations evaluated at the volume that minimizes the energy for each structure. Energies are reported relative to the lowest-energy structure. In the case of quartz, both the left-handed (1) and right-handed (2) structures are reported. Data shown are for the model trained against all available reference data.

Structure (SiO <sub>2</sub> )	DFT (meV atom <sup>-1</sup> )	NEP (meV atom <sup>-1</sup> )
$\alpha$ -quartz-1	0.0	0.0
$\alpha$ -quartz-2	0.3	0.0
$\alpha$ -cristobalite	5.5	6.3
MC-tridymite	7.4	4.1
$\beta$ -quartz-1	7.4	8.4
$\beta$ -quartz-2	7.4	8.4
keatite	7.8	3.1
$\alpha$ -tridymite	10.9	7.6
coesite	12.6	13.2
$\beta$ -tridymite	17.8	18.7
$\beta$ -cristobalite	19.0	18.5
stishovite	139.1	140.7

**Table S4: Elastic stiffness tensors of silicon structures from NEP model.** Elastic stiffness tensors of silicon structures in GPa. Data shown are for the model trained against all available reference data.

Structure	$c_{11}$	$c_{22}$	$c_{33}$	$c_{23}$	$c_{13}$	$c_{12}$	$c_{44}$	$c_{55}$	$c_{66}$
diamond	144.4	144.4	144.4	76.6	76.6	76.6	46.6	46.6	46.6
lonsdaleite	152.6	152.6	176.1	64.2	64.2	70.0	37.3	37.3	41.3
$\beta$ -tin	184.5	184.5	152.7	71.9	71.9	78.9	19.5	19.5	21.6
bc8	157.2	157.2	157.2	56.3	56.3	56.3	40.7	40.7	40.7
simple-hexagonal	145.1	145.1	327.0	47.6	47.6	111.1	19.6	19.6	17.0
fcc	58.4	58.4	58.4	93.1	93.1	93.1	-32.3	-32.3	-32.3

**Table S5: Elastic stiffness tensors of silica structures from NEP model.** Elastic stiffness tensors of silica structures in GPa. Data shown are for the model trained against all available reference data.

Structure	$c_{11}$	$c_{22}$	$c_{33}$	$c_{23}$	$c_{13}$	$c_{12}$	$c_{44}$	$c_{55}$	$c_{66}$
$\alpha$ -quartz-1	86.1	86.0	99.5	12.6	13.1	7.3	56.5	56.5	39.3
$\alpha$ -quartz-2	86.1	86.0	99.5	12.6	13.1	7.3	56.5	56.5	39.3
$\beta$ -quartz-1	200.3	200.3	210.0	131.7	131.7	95.6	-5.0	-5.0	52.4
$\beta$ -quartz-2	200.3	200.3	210.0	131.7	131.7	95.6	-5.0	-5.0	52.4
$\alpha$ -cristobalite	31.8	31.8	33.6	-9.9	-9.9	28.7	66.2	66.2	24.6
$\beta$ -cristobalite	206.1	206.1	206.1	140.0	140.0	140.0	94.4	94.4	94.4
MC-tridymite	71.2	73.3	83.5	-8.4	30.6	3.2	29.2	35.7	24.6
$\beta$ -tridymite	252.2	252.2	278.3	100.3	100.3	136.0	52.9	52.9	58.1
coesite	189.3	247.0	268.2	68.4	92.8	79.5	56.0	74.7	67.0
stishovite	503.9	503.9	921.4	205.3	205.3	400.0	259.5	259.5	490.5

## Supplementary Figures

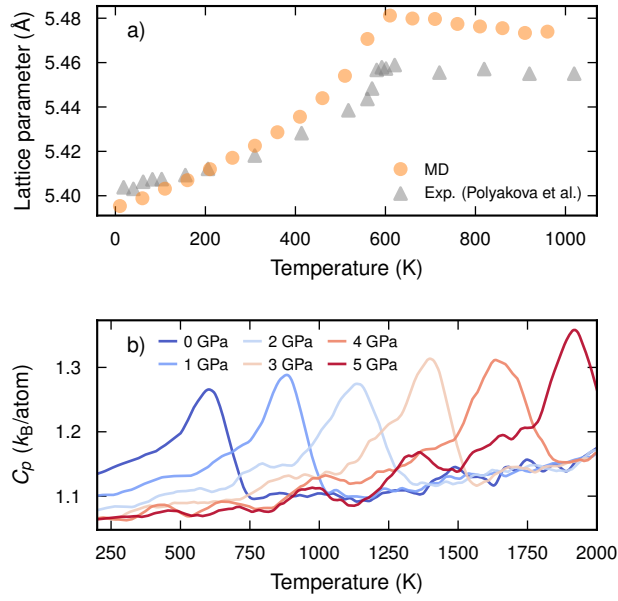


**Fig. S1: Thermal expansion and heat capacity of quartz.** (a) Thermal expansion of quartz at 0 GPa obtained through MD simulations compared to experimental data from Ref. 14. (b) Heat capacity of quartz as a function of temperature at pressures from 0 GPa to 5 GPa. The pronounced peak in each curve indicates the  $\alpha$ - $\beta$ -quartz transition temperature.

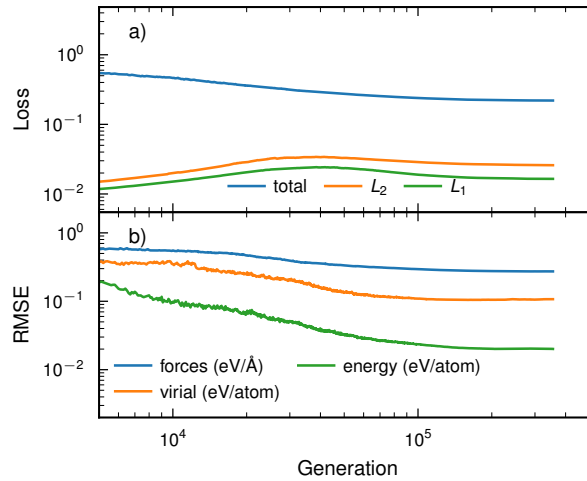


**Fig. S2: Training of NEP model.** Evolution of (a) the total loss function  $\mathcal{L}$  (blue) and the  $\mathcal{L}_1$  (green) and  $\mathcal{L}_2$  norms (orange) of the parameter vector as well as (b) the RMSEs of the energies  $\mathcal{L}_e$  (green), forces  $\mathcal{L}_f$  (blue), and virials  $\mathcal{L}_v$  (orange). The total loss function is given by  $\mathcal{L} = \lambda_1 \mathcal{L}_1 + \lambda_2 \mathcal{L}_2 + \lambda_e \mathcal{L}_e + \lambda_f \mathcal{L}_f + \lambda_v \mathcal{L}_v$ , where  $\lambda_i$  are hyperparameters of the optimization procedure. Data shown are for the model trained against all available reference data.

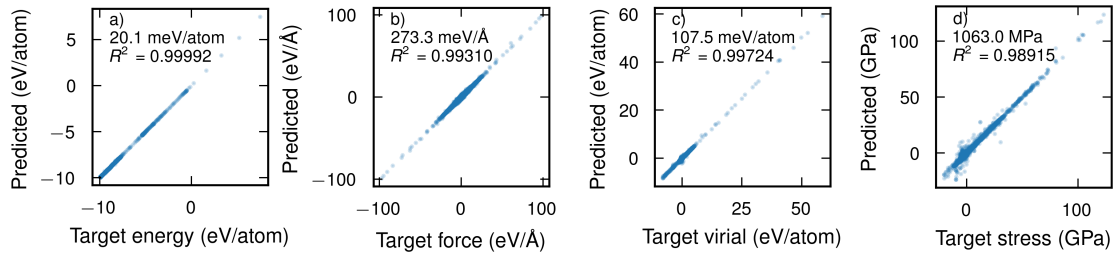


**Fig. S3: Parity plots for NEP model.** Parity plots for (a) energy, (b) forces, (c) virials, and (d) stresses for the machine-learned interatomic potential of the NEP form constructed in this work using all available reference data. The insets indicate the RMSEs and coefficients of correlation ( $R^2$ ).

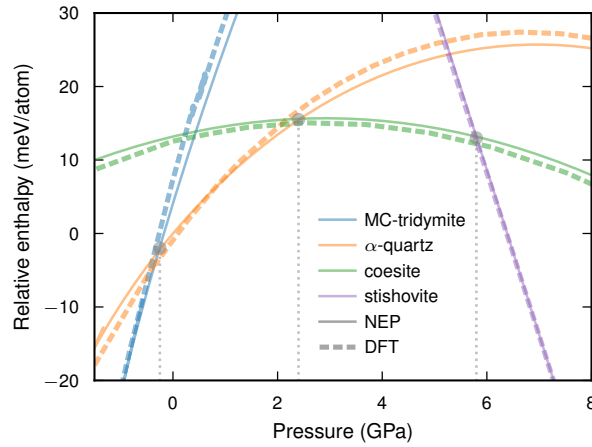


**Fig. S4: Enthalpy-pressure curves from DFT and NEP model.** Enthalpy as a function of pressure. Grey circles indicate intersections of the enthalpy curves, corresponding to zero-temperature phase transitions. Data shown are for the model trained against all available reference data.

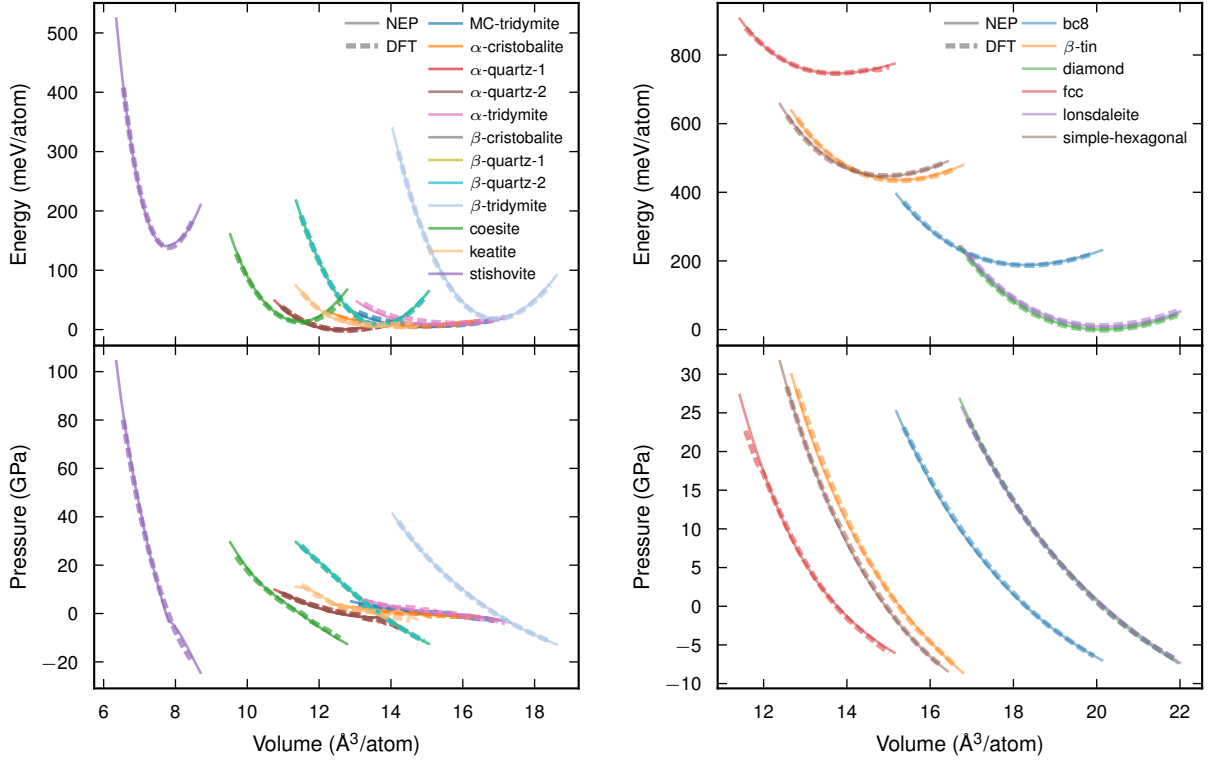


**Fig. S5: Energy-volume and pressure-volume curves from DFT and NEP model.** Energy and pressure as a function of volume for silica and silicon. Data shown are for the model trained against all available reference data.

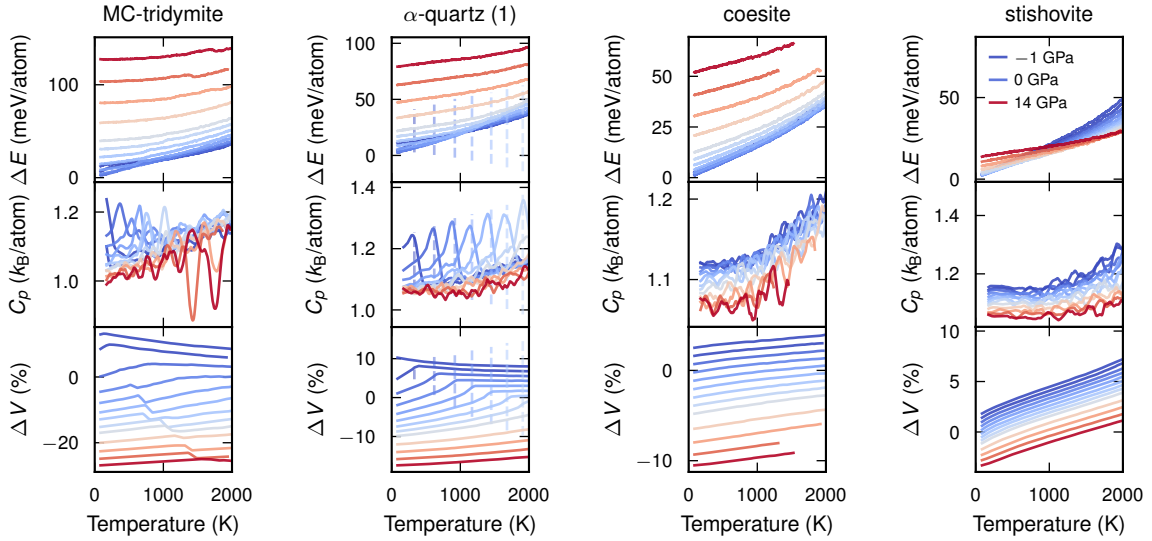


**Fig. S6: Temperature-dependent properties from NEP-MD simulations.** Temperature dependence of potential energy, heat capacity, and volume from classical MD simulations. In the case of the potential energy the 0 K reference energy of the ideal lattice  $E_0$  and the Dulong-Petit part of the heat capacity have been subtracted,  $\Delta E = E - E_0 - 3/2k_B T$ . The change in volume is referenced to the relaxed reference structure,  $\Delta V = V/V_0 - 1$ . Data shown are for the model trained against all available reference data.

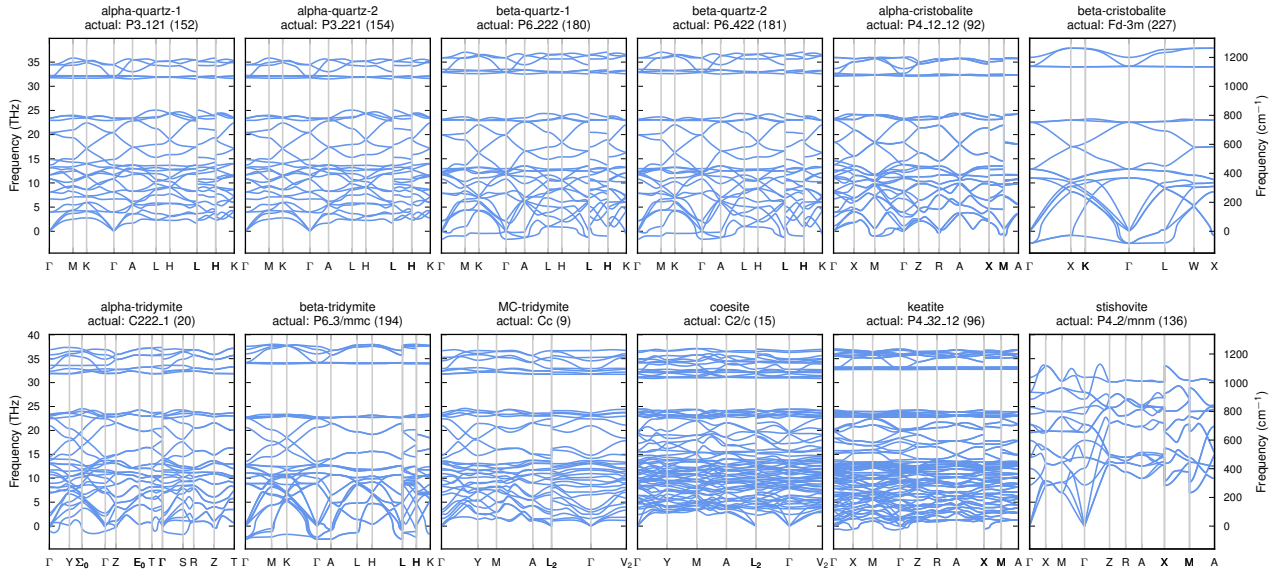


**Fig. S7: Phonon dispersions for silica structures from NEP model.** Data shown are for the model trained against all available reference data.

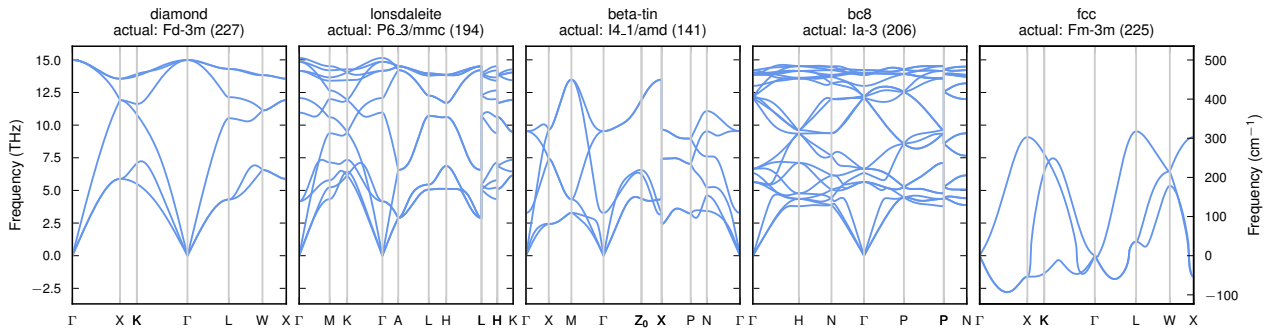


**Fig. S8: Phonon dispersions for silicon structures from NEP model.** Data shown are for the model trained against all available reference data.

- [1] Z. Fan, Z. Zeng, C. Zhang, Y. Wang, K. Song, H. Dong, Y. Chen, and T. Ala-Nissila, *Neuroevolution machine learning potentials: Combining high accuracy and low cost in atomistic simulations and application to heat transport*, Physical Review B **104**, 104309 (2021). doi:10.1103/PhysRevB.104.104309.
- [2] Z. Fan, Y. Wang, P. Ying, K. Song, J. Wang, Y. Wang, Z. Zeng, K. Xu, E. Lindgren, J. M. Rahm, A. J. Gabourie, J. Liu, H. Dong, J. Wu, Y. Chen, Z. Zhong, J. Sun, P. Erhart, Y. Su, and T. Ala-Nissila, *GPUMD: A package for constructing accurate machine-learned potentials and performing highly efficient atomistic simulations*, The Journal of Chemical Physics **157**, 114801 (2022). doi:10.1063/5.0106617.
- [3] K. Xu, H. Bu, S. Pan, E. Lindgren, Y. Wu, Y. Wang, J. Liu, K. Song, B. Xu, Y. Li, T. Hainer, L. Svensson, J. Wiktor, R. Zhao, H. Huang, C. Qian, S. Zhang, Z. Zeng, B. Zhang, B. Tang, Y. Xiao, Z. Yan, J. Shi, Z. Liang, J. Wang, T. Liang, S. Cao, Y. Wang, P. Ying, N. Xu, C. Chen, Y. Zhang, Z. Chen, X. Wu, W. Jiang, E. Berger, Y. Li, S. Chen, A. J. Gabourie, H. Dong, S. Xiong, N. Wei, Y. Chen, J. Xu, F. Ding, Z. Sun, T. Ala-Nissila, A. Harju, J. Zheng, P. Guan, P. Erhart, J. Sun, W. Ouyang, Y. Su, and Z. Fan, *GPUMD 4.0: A high-performance molecular dynamics package for versatile materials simulations with machine-learned potentials*, Materials Genome Engineering Advances **3**, e70028 (2025). doi:10.1002/mgea.70028.

- [4] E. Fransson, J. Wiktor, and P. Erhart, *Phase Transitions in Inorganic Halide Perovskites from Machine-Learned Potentials*, *The Journal of Physical Chemistry C* **127**, 13773 (2023). doi:10.1021/acs.jpcc.3c01542.
- [5] E. Lindgren, J. M. Rahm, E. Fransson, F. Eriksson, N. Österbacka, Z. Fan, and P. Erhart, *calorine: A Python package for constructing and sampling neuroevolution potential models*, *Journal of Open Source Software* **9**, 6264 (2024). doi:10.21105/joss.06264.
- [6] A. Larsen, J. Mortensen, J. Blomqvist, I. Castelli, R. Christensen, M. Dulak, J. Friis, M. Groves, B. Hammer, C. Hargus, E. Hermes, P. Jennings, P. Jensen, J. Kermode, J. Kitchin, E. Kolsbjerg, J. Kubal, K. Kaasbjerg, S. Lysgaard, J. Maronsson, T. Maxson, T. Olsen, L. Pastewka, A. Peterson, C. Rostgaard, J. Schiøtz, O. Schütt, M. Strange, K. Thygesen, T. Vegge, L. Vilhelmsen, M. Walter, Z. Zeng, and K. W. Jacobsen, *The Atomic Simulation Environment – A Python library for working with atoms*, *J. Phys. Condens. Matter* **29**, 273002 (2017). doi:10.1088/1361-648X/aa680e.
- [7] F. Eriksson, E. Fransson, and P. Erhart, *The Hiphive Package for the Extraction of High-Order Force Constants by Machine Learning*, *Advanced Theory and Simulations* **2**, 1800184 (2019). doi:10.1002/adts.201800184.
- [8] P. E. Blöchl, *Projector augmented-wave method*, *Physical Review B* **50**, 17953 (1994). doi:10.1103/PhysRevB.50.17953.
- [9] G. Kresse and D. Joubert, *From ultrasoft pseudopotentials to the projector augmented-wave method*, *Physical Review B* **59**, 1758 (1999). doi:10.1103/PhysRevB.59.1758.
- [10] G. Kresse and J. Hafner, *Ab initio molecular dynamics for liquid metals*, *Physical Review B* **47**, 558 (1993). doi:10.1103/PhysRevB.47.558.
- [11] G. Kresse and J. Furthmüller, *Efficient iterative schemes for ab initio total-energy calculations using a plane-wave basis set*, *Physical Review B* **54**, 11169 (1996). doi:10.1103/PhysRevB.54.11169.
- [12] G. Kresse and J. Furthmüller, *Efficiency of ab-initio total energy calculations for metals and semiconductors using a plane-wave basis set*, *Computational Materials Science* **6**, 15 (1996). doi:https://doi.org/10.1016/0927-0256(96)00008-0.
- [13] J. W. Furness, A. D. Kaplan, J. Ning, J. P. Perdew, and J. Sun, *Accurate and Numerically Efficient r2SCAN Meta-Generalized Gradient Approximation*, *The Journal of Physical Chemistry Letters* **11**, 8208 (2020). doi:10.1021/acs.jpcllett.0c02405.
- [14] I. G. Polyakova, *4. The Main Silica Phases and Some of Their Properties*, in *4. The Main Silica Phases and Some of Their Properties* (De Gruyter, 2014), p. 197. doi:10.1515/9783110298581.197.